Bio-Design and Manufacturing (2022) 5:641–659
https://doi.org/10.1007/s42242-022-00207-1

RESEARCH ARTICLE

Rapid and mass manufacturing of soft hydrogel microstructures for cell patterns assisted by 3D printing

Chaofan He[1] · Xuechun Chen[2] · Yuan Sun[1] · Mingjun Xie[1] · Kang Yu[1] · Jing He[1] · Jinwei Lu[3] · Qing Gao[1] · Jing Nie[1] · Yi Wang[2,7] · Yong He[1,4,5,6]

Received: 25 February 2022 / Accepted: 20 July 2022 / Published online: 2 September 2022

Abstract

Micro-/nano-patterns on hydrogels are widely used in cell patterning. However, manufacturing molds with traditional lithography is time-consuming and expensive. In addition, the excessive demolding force can easily damage patterns since biocompatible hydrogels are ultra-soft or brittle. Here, we presented a novel method for rapid and mass fabrication of cell patterns. High-precision three-dimensional (3D) printing was used to manufacture a mold with a resolution of 2 μm, and the gelatin-based hydrogel was cured by thermal–photo-crosslinking so that the low-concentration and low-substitution-rate hydrogel could be demolded successfully. We found that pre-cooling before illumination made gelatin-based hydrogels resilient due to the partial regain of triple-helix structures . With this method, arbitrarily customized hydrogel patterns with a feature size of 6–80 μm can be fabricated stably and at low cost. When cardiomyocytes were seeded on ultra-soft hydrogels with parallel groove structures, a consistent and spontaneous beating with 216 beats per minute (BPM) could be observed, approaching the natural beating rate of rat hearts (300 BPM). Overall, this work provides a general scheme for manufacturing cell patterns which has great potential for cell ethology and tissue repair.

Chaofan He and Xuechun Chen have contributed equally to this work.

✉ Yi Wang
zjuwangyi@zju.edu.cn

✉ Yong He
yongqin@zju.edu.cn

1 State Key Laboratory of Fluid Power and Mechatronic Systems, School of Mechanical Engineering, Zhejiang University, Hangzhou 310027, China

2 Pharmaceutical Informatics Institute, College of Pharmaceutical Sciences, Zhejiang University, Hangzhou 310058, China

3 Department of Orthopedic Surgery, The Second Affiliated Hospital, School of Medicine, Zhejiang University, Hangzhou 310009, China

4 Key Laboratory of Materials Processing and Mold, Zhengzhou University, Zhengzhou 450002, China

5 Key Laboratory of 3D Printing Process and Equipment of Zhejiang Province, College of Mechanical Engineering, Zhejiang University, Hangzhou 310027, China

6 Cancer Center, Zhejiang University, Hangzhou 310058, China

7 State Key Laboratory of Component-Based Chinese Medicine, Tianjin University of Traditional Chinese Medicine, Tianjin 300072, China

Graphic abstract

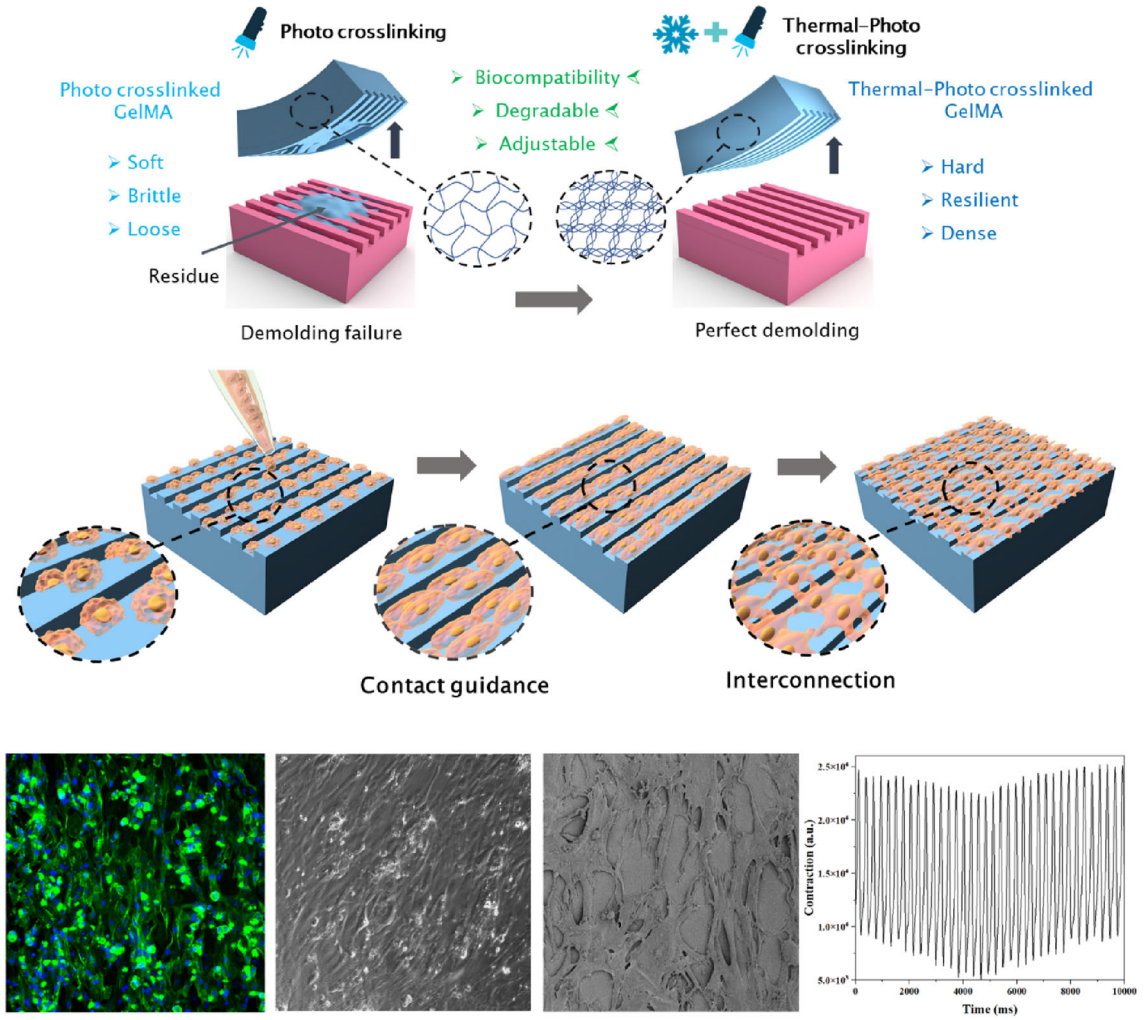

Keywords 3D printing · Gelatin-based hydrogel · Cell pattern · Cardiomyocytes beating

Introduction

The interaction between materials and cells is a research hotspot in tissue engineering and regenerative medicine. In addition to its biochemical characteristics, the topology of a material surface has an important impact on cell behaviors. Many studies have shown that micro-/nano-structures close to the cell size have a "contact guidance" effect on cells [1–4]; that is, the growth orientation of cells tends to be consistent with the structures. This has been verified in many cell species such as myoblasts [5], fibroblasts [6], osteoblasts [7], and epithelia [8]. With the development of micro-/nano-manufacturing technologies, researchers have been able to build specific microscale bionic topology to control a series of cell behaviors such as proliferation, migration, and differentiation according to different biomedical requirements, which opens wide prospects for application in the repair of highly oriented tissues such as muscle, nerve, and tendon.

However, most of the existing studies on cell–substrate interactions are based on materials with poor biocompatibility such as polydimethylsiloxane (PDMS), silicon, and quartz [3, 9–12] rather than biomaterials with better biocompatibility. This is mainly because finding a way to fabricate delicate micro-/nano-structures on soft or brittle hydrogels is still a great challenge. Although several additive manufacturing technologies such as digital light processing (DLP) and two-photon polymerization (TPP) have been used to fabricate micro-/nano-structures on hard materials, it is still difficult to guarantee the structural fidelity of hydrogels [13]. Lithography technology is mainly aimed at semiconductors [14], quartz, and glass [15]. High-resolution patterned hydrogels

have also been produced using nanoimprint lithography technology [16, 17], but the high cost and complex operation process limit the applications of this method. Therefore, cast molding is a more feasible fabrication method for hydrogel surface microstructures due to its versatility, simplicity, and low requirements for laboratory environments [18–20]. Many studies have reported the use of casting molding methods to produce various micropatterned hydrogels with relatively high mechanical strength, such as alginate [21] and silk protein [22]. Nevertheless, since gelatin-based hydrogels are usually soft and brittle, the excessive demolding force can easily cause structural damage. Although some studies have achieved fabrication of micropatterned gelatin-based hydrogels, they were all based on a high grafting rate [23] or high-concentration [24] materials. It has also been reported that sacrificial materials [25], assisted solvent techniques [26], and flexible fiber [27] were used for demolding. It is still a challenge to fabricate arbitrarily customized microstructures with a rapid, simple, and low-cost method.

Improving the mechanical strength of hydrogels can effectively prevent demolding failure. For methacrylate gelatin (GelMA), increasing the grafting rate can improve the crosslinking density and mechanical properties, but it also destroys the amino acid sequence, resulting in lowered biocompatibility [28]. Increasing the concentration reduces water content and also affects cell activity. Another strategy is to add another component, such as hyaluronic acid (HA) [29], alginate [30], poly(ethylene glycol)diacrylate (PEGDA) [31], methacrylated chitosan (CSMA) [32], or dextran glycidyl methacrylate (DexMA) [33]. However, the addition of these reinforcing phases is often very cumbersome and brings many obstacles to the manufacturing process. Therefore, it is very valuable to use a simple and low-cost method to improve the mechanical strength of GelMA while ensuring good biocompatibility.

Here, a new method is proposed to realize rapid and mass manufacturing of soft hydrogel microstructures. First, we manufactured a male mold with ultra-precision structures by high-precision DLP printing. Compared with lithography technology, it significantly reduced cost and greatly improved design flexibility. Then, we fabricated a PDMS female mold by casting molding. Finally, the GelMA solution was cast on the PDMS mold with thermal–photo-crosslinking. Compared with photo-crosslinked GelMA (PGelMA), thermal–photo-crosslinked GelMA (TPGelMA) is harder, denser, and more ductile, while maintaining satisfactory biocompatibility, degradability, and adjustability. The basic molecular unit of collagen, the triple-helix structure (THS) [34–36], endows GelMA with reversible thermal crosslinking characteristics [37, 38]. When temperature is decreased, partial regain of the THS leads to the solution–gelation transition of GelMA [39]. A GelMA with permanent THS, that is TPGelMA, can be obtained by ultraviolet (UV) curing with cooling. The increased mechanical properties of TPGelMA greatly reduce the risk of structural damage during the stripping process.

With this method, cell patterns can be obtained quickly and stably, which was verified with cardiomyocytes, tendon stem cells, and fibroblasts. Interestingly, due to the outstanding biological characteristics of gelatin-based hydrogels, the cells arranged longitudinally as well as interconnecting transversely and formed a cell network. The cardiomyocyte patterns beat consistently and spontaneously with 216 beats per minute (BPM) over a large area. The spontaneous beating rate reported in many previous studies is lower than 100 BPM [40–43]. This result has broad application potential in cell ethology, bionic tissue construction, and drug screening. In addition, this method may become a universal manufacturing method for microfluidic chips and microneedles based on hydrogels (Fig. 1).

Results

Formation principle of the thermal–photo-crosslinking network

In order to better simulate the in vivo environment and observe cell behaviors, a variety of biomaterials with excellent properties have been developed, such as GelMA [44], methacryloyl hyaluronic acid (HAMA) [45], alginate [46], PEGDA [47], and silk fibroin [48]. Among them, gelatin-based hydrogels such as GelMA have become more and more popular for their excellent biocompatibility. GelMA is a polypeptide material obtained by hydrolytic degradation and chemical modification of naturally occurring collagen. Collagen is a component of the extracellular matrix, which gives GelMA its good cell adhesion [49] and degradability [50]. In addition, the covalent crosslinking of GelMA under UV irradiation makes it easy to form specific patterns, morphologies, and three-dimensional (3D) structures [51, 52]. Because of these two points, GelMA is widely used in tissue engineering [53, 54], cell-behavior regulation [55–57], organs-on-a-chip [27, 58–60], and drug screening [61].

In the process of GelMA photo-curing, the photo-initiator is converted from the ground state to the excited state under UV irradiation. It induces the methacrylic acid (MA) group on GelMA to form a covalently crosslinked hydrogel. Meanwhile, the highly similar structures of GelMA and gelatin cause it to form the THS and random coils through the hydrogen bond between the amide group and carbonyl group at low temperatures (Fig. 2A). It gives GelMA unique reversible thermal crosslinking characteristics. Then, the irreversible composite crosslinking network can be obtained by thermal–photo-crosslinking. This denser network leads to better mechanical properties of TPGelMA.

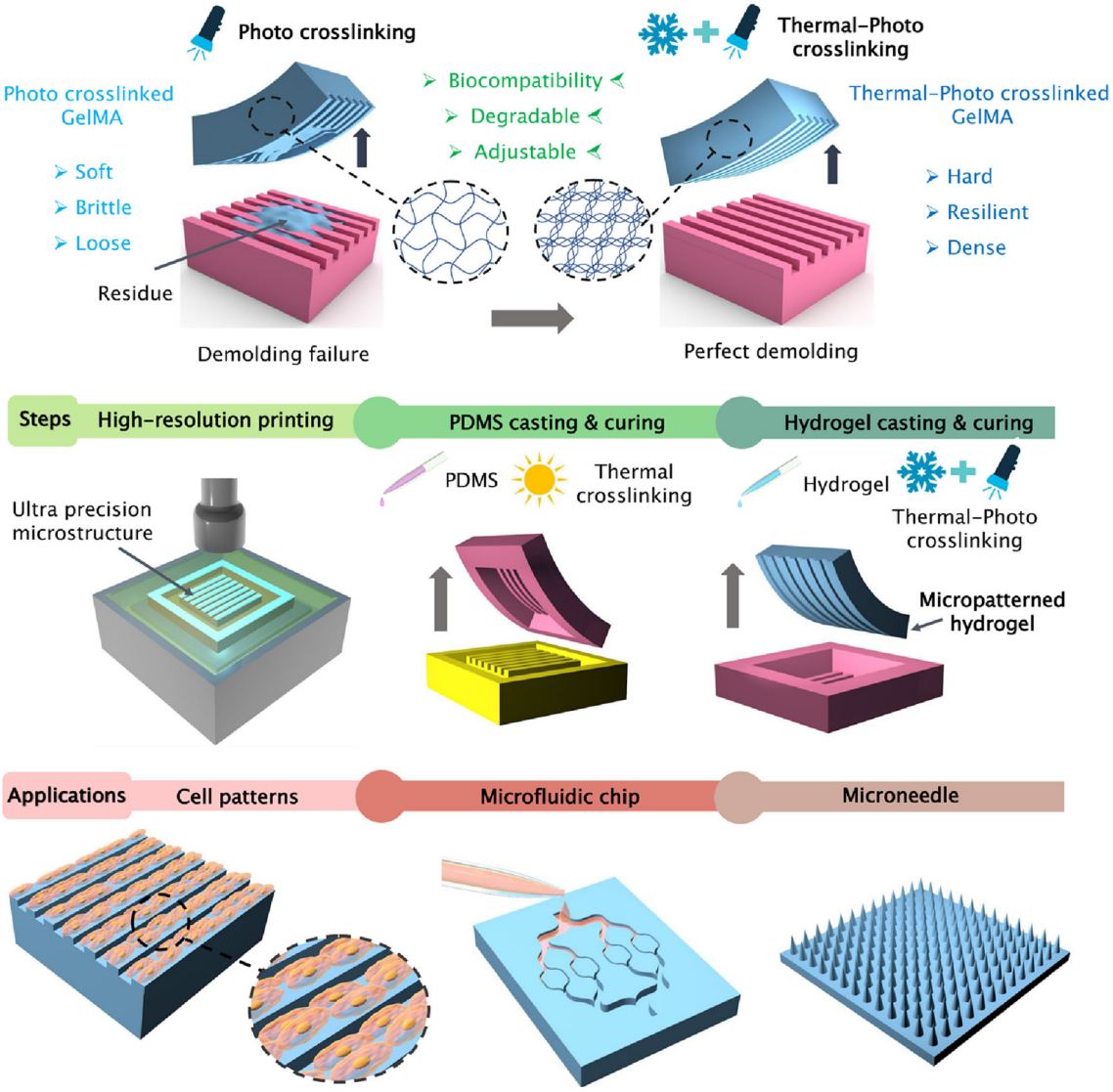

Fig. 1 Schematic for fabrication of gelatin-based hydrogel microstructures and their application

The circular dichroism (CD) spectrum is often used to detect the secondary structure of proteins. The CD spectra of GM30, GM60, GM90 are compared in Fig. 2B. All three lines have a negative peak near 198 nm, which is similar to collagen [62]. The amplitude of the peak decreased when the substitution rate increased, indicating that the introduction of MA groups destroyed the original amino acid sequence of the gelatin chain and hindered formation of THS. The CD spectra of GM30 at different temperatures also showed that the formation of THS was promoted by decreasing temperature (Fig. 2C). Fourier transform infrared reflection (FTIR) analysis showed that the peak of the TPGelMA spectrum was higher and the frequency also changed significantly, which was closely related to the increase in the number of hydrogen bonds (Fig. 2D) [63].

In terms of mechanical strength, TPGelMA has a higher Young's modulus (Fig. 2E) and tensile strength (Fig. 2F) than PGelMA. For 15% GM30, the Young's modulus and tensile strength of TPGelMA are 5 and 12 times higher than those of PGelMA, respectively. For 15% GM1M, these values were reduced to 2 and 4, respectively. As the substitution rate increased, the rate of strength increase gradually went down, showing that the introduction of MA group hindered the formation of THS; this was consistent with the results of CD spectra. These two kinds of GelMA also had different volume change rates in different solvents (Fig. 2G). The results showed that the volume change of TPGelMA in deionized water, phosphate-buffered saline (PBS) solution, and 75% alcohol solution was significantly less than that of PGelMA, indicating that the molecular network of TPGelMA was more compact.

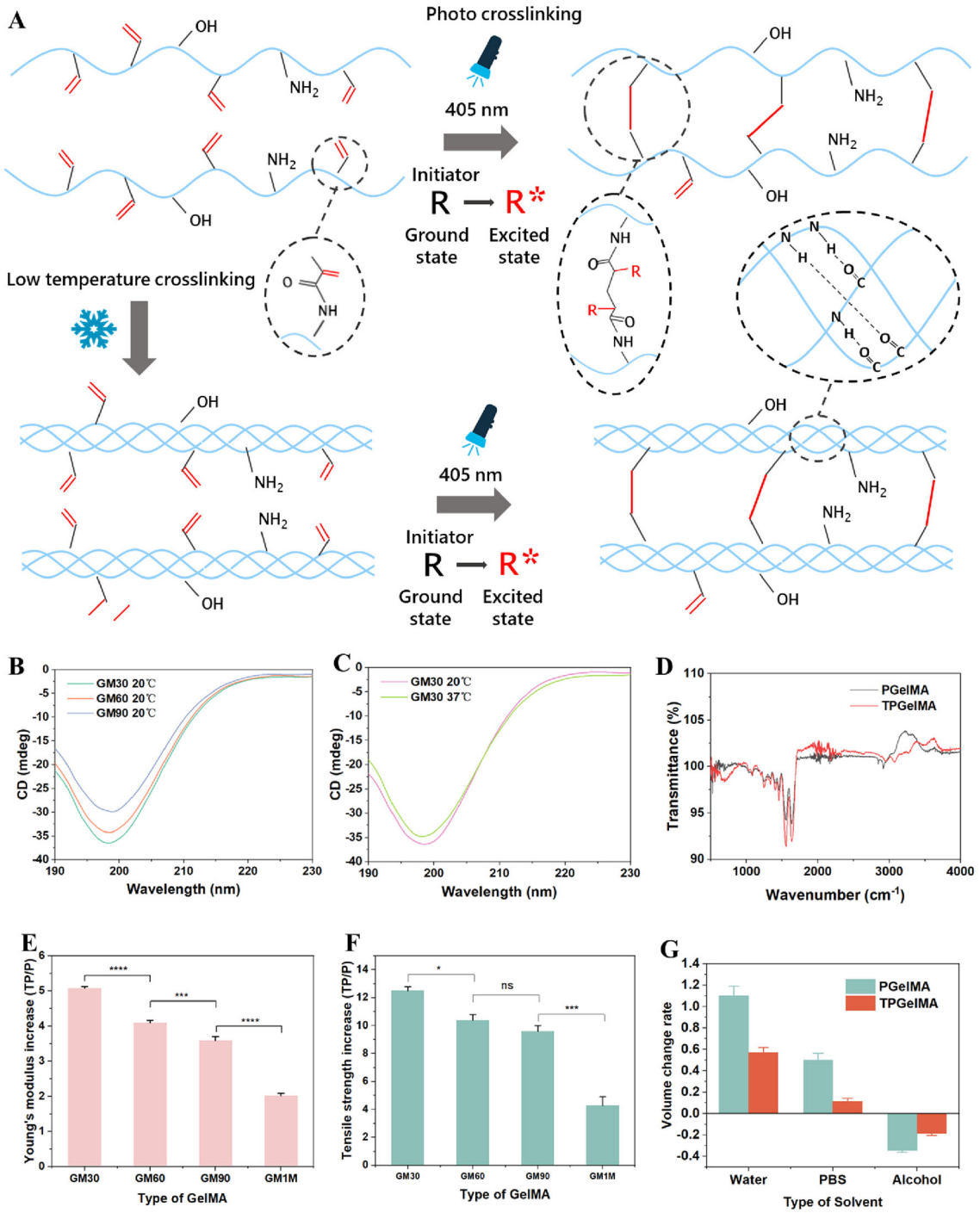

Fig. 2 Formation and characteristics of the photo and thermal crosslinking network of GelMA. **A** Formation principle of photo-crosslinking and thermal–photo-crosslinking network. **B** CD spectra of 0.02% GM30, GM60, and GM90 at 20 °C. **C** CD spectra of 0.02% GM30 at 20 °C and 37 °C. **D** FTIR analysis of PGelMA and TPGelMA. The ratio of Young's modulus **E** and tensile strength **F** of TPGelMA to PGelMA. **G** Volume change rate of two kinds of GelMA in different solvents. (One-way ANOVA, Tukey's, ns $p>0.05$, *$p<0.05$, **$p<0.01$, ***$p<0.001$, ****$p<0.0001$)

Mechanical test and establishment of hydrogel constitutive model

The wet, soft, and brittle properties of hydrogels make it difficult to measure the mechanical data accurately. So far, most of the research on the mechanical properties of hydrogels has been focused on the compression test, which is not comprehensive or systematic. To solve this problem, we designed a series of experimental schemes to obtain various mechanical data on the hydrogels. Based on this, we established adhesion and damage constitutive models of the hydrogels during demolding.

A dumbbell-shaped hydrogel specimen was designed for tensile tests (Fig. 3Ai). The results showed that Young's modulus, tensile strength, and elongation at break of TPGelMA were significantly improved (Fig. 3Aii). After the strain reached 200%, the slope of the stress–strain curve increased significantly, which is called the "strain hardening" [64] effect. Interestingly, this phenomenon did not occur in PGelMA. Throughout the tensile process, the stress–strain curve of PGelMA remained linear. It may be that its molecular network was relatively loose and broke before the molecular chain orientation tends to be consistent.

The high moisture content of hydrogels makes its surface very wet and slippery and the shear test method for hard materials is not applicable. Therefore, we designed a shear test scheme assisted by resin fixtures (Fig. 3Bi). Both resin and GelMA cross link through covalent bonds, while the resin has more covalent binding sites than GelMA. Therefore, compared with the GelMA material inside, the GelMA–resin interface formed a denser network. During the shear test, the inside of the GelMA material was destroyed first, which enabled us to obtain accurate shear data. The results showed that TPGelMA had a higher shear strength and shear modulus (Fig. 3Bii).

Similarly, the covalent crosslinking properties of resin and GelMA were used in the test of normal adhesion (Fig. 3Ci) and tangential adhesion (Fig. 3Di). It should be noted that the crosslinking principle of PDMS is different, so it is inert and has almost no crosslinking reaction with GelMA. Therefore, the interfacial bonding strength of the GelMA-PDMS interface is much lower than that of the GelMA–resin interface. In the normal adhesion test, the separation force and separation displacement of TPGelMA were larger than those of PGelMA (Fig. 3Cii). However, in the tangential adhesion test, the separation force of TPGelMA was close to that of PGelMA, but the separation displacement was much smaller (Fig. 3Dii).

Since the normal and tangential adhesion behaviors of GelMA were highly linear, the linear elastic traction separation model was used to describe the cohesive behavior during the stripping process (Fig. 3E).

$$\boldsymbol{t} = \begin{bmatrix} t_{\mathrm{n}} \\ t_{\mathrm{s}} \\ t_{\mathrm{t}} \end{bmatrix} = \begin{bmatrix} K_{\mathrm{nn}} & K_{\mathrm{ns}} & K_{\mathrm{nt}} \\ K_{\mathrm{ns}} & K_{\mathrm{ss}} & K_{\mathrm{st}} \\ K_{\mathrm{nt}} & K_{\mathrm{st}} & K_{\mathrm{tt}} \end{bmatrix} \begin{bmatrix} \delta_{\mathrm{n}} \\ \delta_{\mathrm{s}} \\ \delta_{\mathrm{t}} \end{bmatrix} = \boldsymbol{K}\boldsymbol{\delta}, \tag{1}$$

where $\boldsymbol{t}$ is the nominal traction stress vector, consisting of three components (t_{n}, t_{s}, t_{t}) which represent the normal and two shear tractions, respectively. The corresponding separation vector is $\boldsymbol{\delta}$, which consists of δ_{n}, δ_{s}, and δ_{t}. $\boldsymbol{K}$ represents the stiffness vector in different directions.

Usually, the normal and tangential stiffness components are not coupled. This means that pure normal separation does not produce cohesion force in the shear direction and pure shear slip also does not produce any cohesion force in the normal direction. Therefore, the terms K_{nn}, K_{ss}, and K_{tt} need to be defined and the values of other terms are zero.

$$K_{\mathrm{ns}} = K_{\mathrm{nt}} = K_{\mathrm{st}} = 0. \tag{2}$$

In the linear elastic traction separation model, the stiffness in three directions can be defined as

$$\begin{cases} K_{\mathrm{nn}} = t_{\mathrm{n}}^{\mathrm{t}}/\delta_{\mathrm{n}}^{\mathrm{o}}, \\ K_{\mathrm{ss}} = t_{\mathrm{s}}^{\mathrm{t}}/\delta_{\mathrm{s}}^{\mathrm{o}}, \\ K_{\mathrm{tt}} = t_{\mathrm{t}}^{\mathrm{t}}/\delta_{\mathrm{t}}^{\mathrm{o}}, \end{cases} \tag{3}$$

where $t_{\mathrm{n}}^{\mathrm{t}}$ is maximum normal separation force and $t_{\mathrm{s}}^{\mathrm{t}}$, $t_{\mathrm{t}}^{\mathrm{t}}$ are maximum tangential separation force. $\delta_{\mathrm{n}}^{\mathrm{o}}$ is normal initial separation displacement and $\delta_{\mathrm{s}}^{\mathrm{o}}$, $\delta_{\mathrm{t}}^{\mathrm{o}}$ are tangential initial separation displacement. In addition, for isotropic materials

$$K_{\mathrm{ss}} = K_{\mathrm{tt}}. \tag{4}$$

Quadratic separation criterion was used to define damage initialization.

$$\left(\frac{\langle \delta_{\mathrm{n}} \rangle}{\delta_{\mathrm{n}}^{\mathrm{o}}}\right)^2 + \left(\frac{\delta_{\mathrm{s}}}{\delta_{\mathrm{s}}^{\mathrm{o}}}\right)^2 + \left(\frac{\delta_{\mathrm{t}}}{\delta_{\mathrm{t}}^{\mathrm{o}}}\right)^2 = 1, \tag{5}$$

where δ_{n} is used to signify that a purely compressive displacement does not initiate damage.

The Benzeggagh–Kenane form was used to describe damage evolution (Fig. 3F).

$$G_{\mathrm{n}}^{\mathrm{C}} + \left(G_{\mathrm{s}}^{\mathrm{C}} - G_{\mathrm{n}}^{\mathrm{C}}\right)\left(\frac{G_{\mathrm{S}}}{G_{\mathrm{T}}}\right)^{\eta} = G^{\mathrm{C}}, \tag{6}$$

where $G_{\mathrm{n}}^{\mathrm{C}}$ and $G_{\mathrm{s}}^{\mathrm{C}}$ represent the critical fracture energies required to cause failure in the normal and the shear directions, respectively. η is a cohesive property parameter.

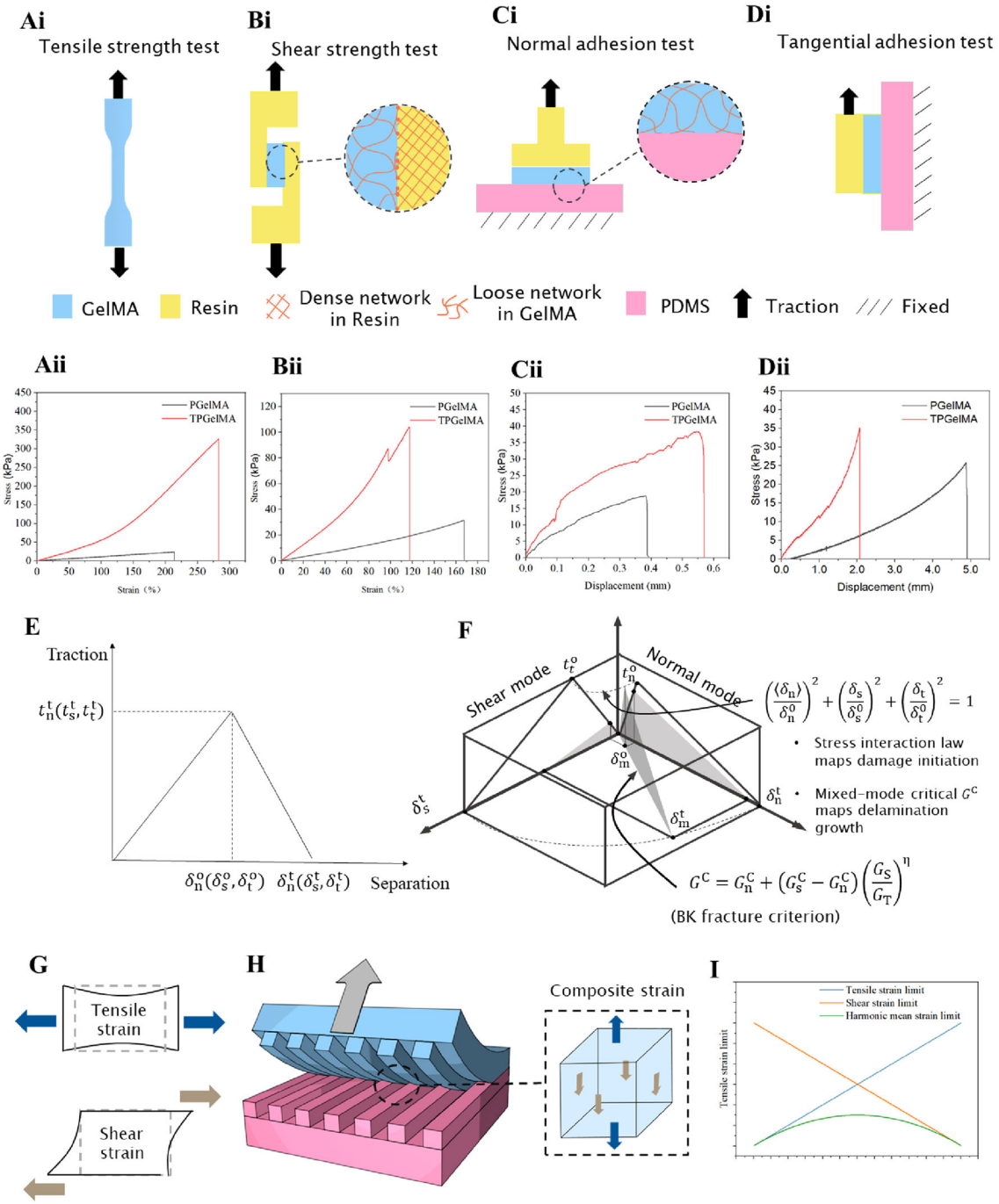

Fig. 3 Mechanical test of hydrogels and establishment of constitutive model. Mechanical tests of tensile strength **Ai**, shear strength **Bi**, normal adhesion **Ci**, and tangential adhesion **Di**, respectively, and **Aii**–**Dii** are the results of these tests, respectively. **E** Contact cohesive behavior model based on linear elastic traction–separation. **F** Damage initialization model based on quadratic separation criterion. **G** Schematic of normal and tangential strains. **H** Composite strain of material element in demolding process. **I** Harmonic average of tensile strain limit and shear strain limit

$$\begin{cases} G_{\mathrm{n}}^{\mathrm{C}} = \frac{1}{2}\left(\frac{t_{\mathrm{n}}^{\mathrm{t}}}{A}\right)\cdot\delta_{\mathrm{n}}^{\mathrm{t}}, \\ G_{\mathrm{s}}^{\mathrm{C}} = \frac{1}{2}\left(\frac{t_{\mathrm{s}}^{\mathrm{t}}}{A}\right)\cdot\delta_{\mathrm{s}}^{\mathrm{t}}, \end{cases} \tag{7}$$

$$G_{\mathrm{S}} = G_{\mathrm{s}} + G_{\mathrm{t}}, \tag{8}$$

$$G_{\mathrm{T}} = G_{\mathrm{n}} + G_{\mathrm{S}}, \tag{9}$$

where G_n, G_s, and G_t are the work done by the tractions in three directions.

$$\begin{cases} G_n = \frac{1}{2}\left(\frac{t_n^t}{A}\right)\cdot\delta_n^o, \\ G_s = G_t = \frac{1}{2}\left(\frac{t_s^t}{A}\right)\cdot\delta_s^o. \end{cases} \tag{10}$$

The two basic strain modes of materials are tensile strain and shear strain (Fig. 3G). Generally, they are different under the same stress. The actual demolding process usually involves pulling the material from an edge. In this process, the stress and strain in different areas are very complex. But to simplify, each material element has tensile strain and shear strain at the same time (Fig. 3H), but in different proportions. For uniformly applied tension and isotropic materials, the harmonic critical failure strain with the same weight was used as the damage criterion. Harmonic averaging considers the effects of both strains and is very sensitive to extreme values, which is consistent with the actual failure behavior. This is similar to the "bucket effect". The weaker side determines the overall performance. The tensile strength of GelMA is clearly higher than the shear strength. Therefore, when the hydrogel is subjected to complex stress, the shear stress limit is reached first, and the existence of tensile strain will further reduce the shear stress limit, which is consistent with the meaning of harmonic average representation (Fig. 3I).

$$\frac{1}{\varepsilon_{max}} = \frac{1}{\varepsilon_n^c} + \frac{1}{\varepsilon_s^c}, \tag{11}$$

where ε_n^c and ε_s^c are the normal stress limit and shear stress limit, respectively. ε_{max} is the harmonic mean strain limit.

Material damage analysis during demolding

The adhesion and damage constitutive models based on hydrogel materials were established to analyze the mechanical behavior of GelMA during the demolding process. Since the material is subjected to both tangential and normal adhesion (Fig. 4Aii), the strain on different surfaces is also different. For systematic discussion, the material–mold contact area was divided into four surfaces: TOP, BOTTOM, SIDE, and CORNER (Fig. 4Aiii). In addition, based on the angle between the demolding force and microstructures, the demolding method was divided into two modes: forward pulling (FP) (θ=0°) and lateral pulling (LP) (θ=90°) (Fig. 4Ai). Obviously, for the simple groove structure, FP is the best scheme, but it is not always so simple in the fabrication of microstructures. These two directions were selected to form an orthogonal datum, and complex situations could then be characterized by the combination of these two directions.

ABAQUS software was used for simulation analysis, and the results showed that the microstructures on PGelMA were seriously damaged (Fig. 4Bi), while the microstructures on TPGelMA remained intact (Fig. 4Bii). For PGelMA, in the process of FP, more than half of the material units on the contact surface were damaged, and the damage was mainly concentrated on the TOP. It might have been caused by the stress concentration effect. In addition, the material deformation of the BOTTOM and CORNER was very similar, but the SIDE was very different. This showed that the BOTTOM and CORNER had similar stress conditions since the force was applied evenly in FP, but the SIDE was mainly affected by shear force (Fig. 4C). In the process of LP, more than half of the material units were still damaged, but the deformation of different surfaces had also changed greatly due to very uneven application of force. The material damage still mainly occurred on the TOP, but almost no material was damaged on the BOTTOM. At the same time, the material deformation of the CORNER was different from that of the BOTTOM, but closer to that of the SIDE (Fig. 4D). In contrast, TPGelMA exhibited much better demolding quality. Neither FP nor LP caused serious structural damage. Similar to PGelMA, the material damage mainly occurred on the TOP, and the other three surfaces remained intact during stripping (Figs. 4E and 4F). Interestingly, in the process of LP, the material deformation of the BOTTOM and CORNER became similar, which showed that the stress conditions of these two surfaces were very similar.

On the whole, the strain of PGelMA was significantly larger in the demolding process, up to 400%, while the maximum strain of TPGelMA was about 70%; this was consistent with the tangential adhesion test data. The higher strength of TPGelMA enabled rapid and stable production of micropatterned hydrogels. During each working process, the residue caused by material damage affects the fidelity of microstructures, which in turn seriously affects quality and efficiency. However, our scheme could realize multiple demolding without cleaning. Good demolding quality could not only reduce the failure rate but also the number of mold cleanings required.

Fabrication of hydrogel surface microstructures

3D printing has great economic benefits and production efficiency. It is a very flexible method of customizing the required structures and shapes with higher fault tolerance. In this study, the male mold could be inverted several times to make the duplicate female molds, which is a very important factor for standardized batch manufacturing. For lithography technology, even if the resolution is high enough, uncontrollable disturbances will occur in each manufacturing process, making it impossible to fully guarantee consistency between two batches. It is worth mentioning that DLP printing also

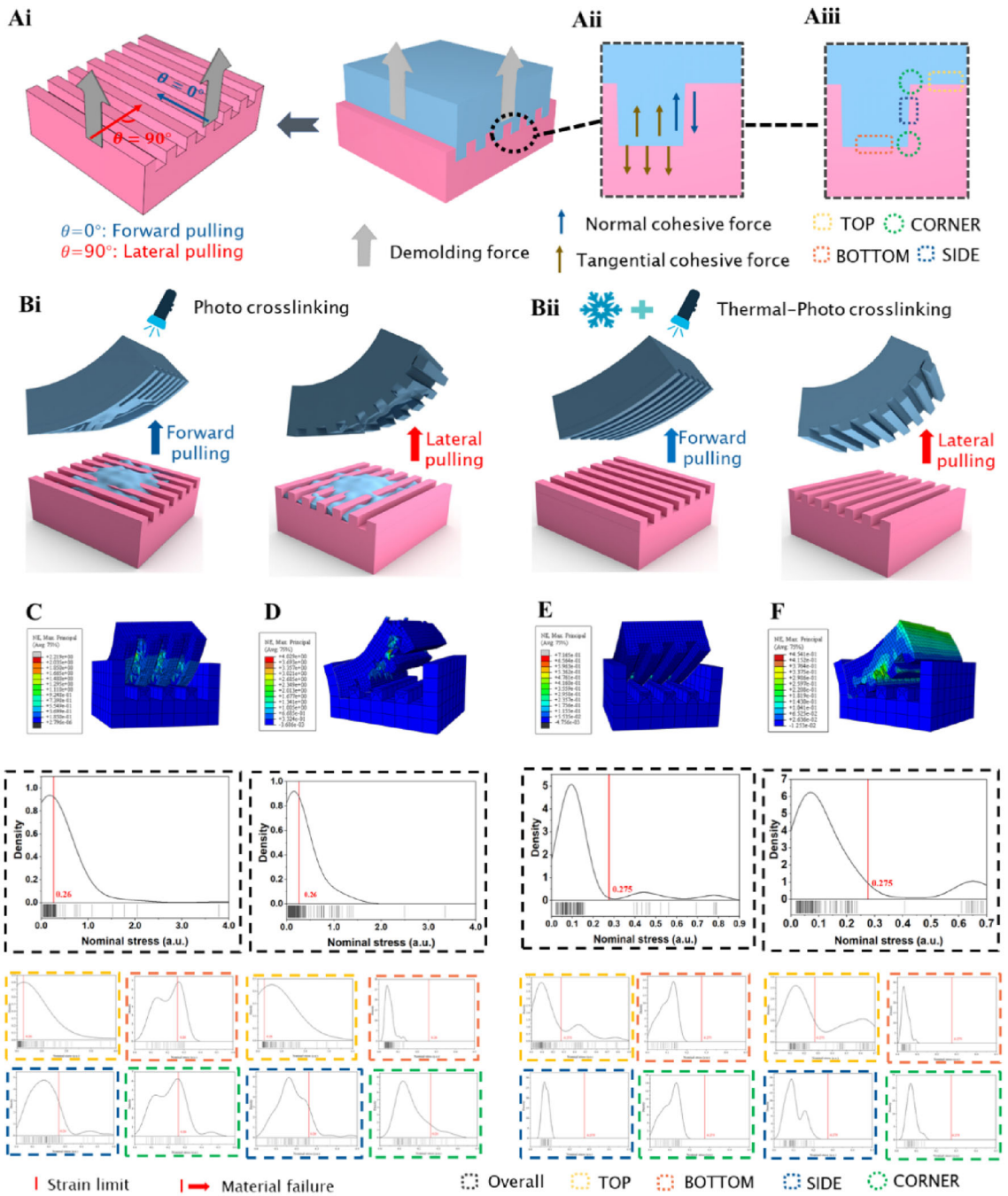

Fig. 4 Effect of pulling direction and crosslinking method on demolding quality. **Ai** The angle between demolding force and microstructures. **Aii** Normal and tangential adhesion during demolding process. **Aiii** Characteristic contact surface during material stripping. **Bi** Schematic of PGelMA demolding process. **Bii** Schematic of TPGelMA demolding process. Simulation results for PGelMA FP **C**, PGelMA LP **D**, TPGelMA FP **E**, and TPGelMA LP **F**. The dashed borders of different colors represent different surfaces. The red vertical line indicates the strain limit, and the right side of the red line indicates that the material unit is damaged

has considerable advantages in building cross-scale structures. The feature of layer-by-layer accumulation makes it possible to construct a customized structure at any scale and complexity level in one exposure. In contrast, it is quite time-consuming to build cross-scale structures with lithography.

We designed a parallel microgroove mold with a depth and width of 10 μm to verify the feasibility of the fabrication

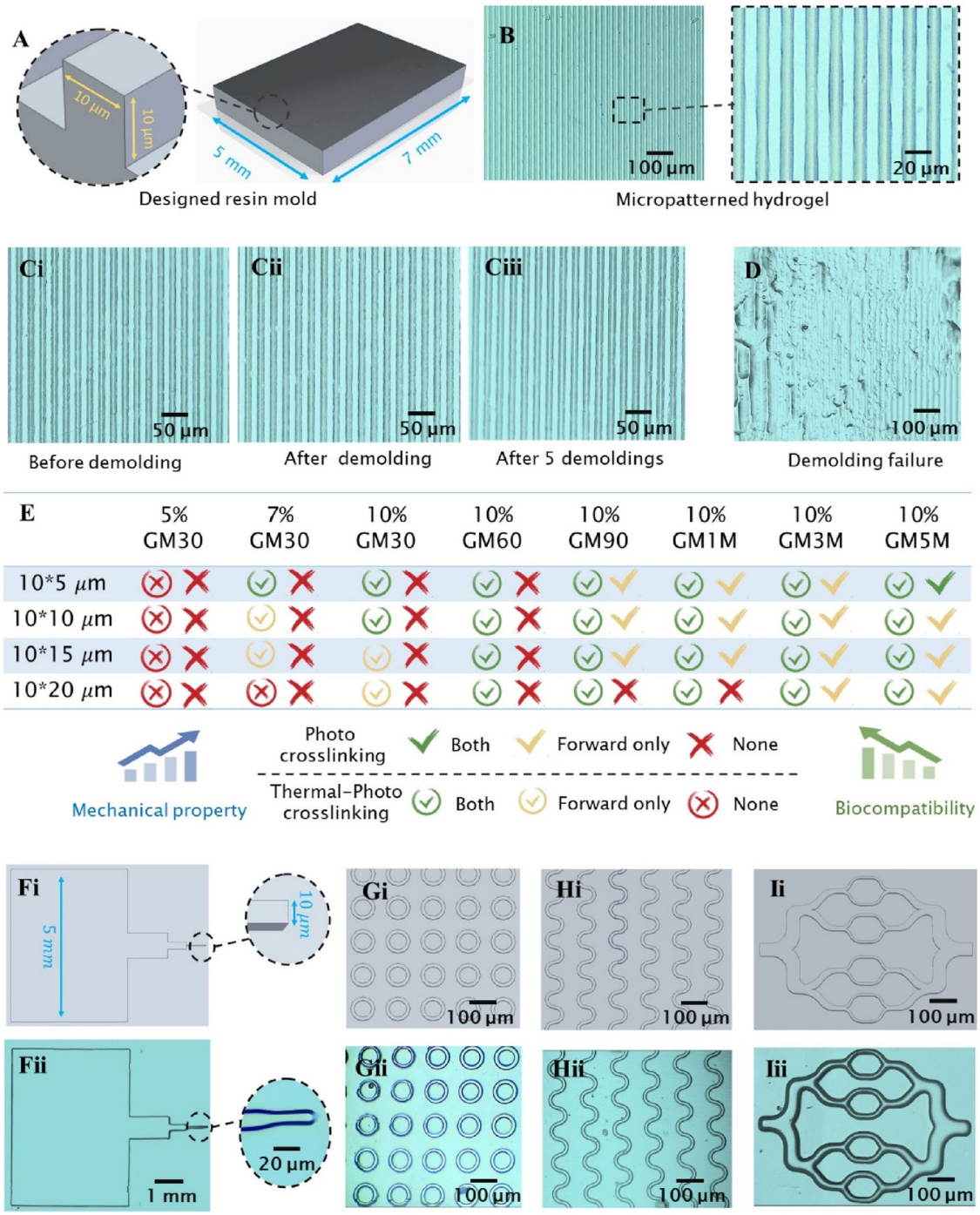

Fig. 5 Fabrication of hydrogel surface microstructures. **A** Resin mold with parallel microgroove structures, in which the width and depth of the groove are both 10 μm. **B** Parallel groove microstructures on hydrogels. **Ci–Ciii** are optical microscope views of the PDMS mold before, after, and after five demoldings, respectively. **D** Hydrogel with demolding failure. **E** Process window of demolding for two crosslinking schemes and pulling directions. **Fi–Ii** Design patterns of different structures. **Fii–Iii** Actual patterns of these structures

scheme (Fig. 5A). A 10-mm-class macroscale is enough to meet most application scenarios of biofabrication. TPGelMA with microstructures was made intact (Fig. 5B), while the microstructure on PGelMA was severely damaged and difficult to distinguish (Fig. 5D). In addition, the same PDMS mold was demolded several times to verify the integrity of the

hydrogel in each process. The results showed that there was no residue on the mold after demolding (Figs. 5Ci and 5Cii). Consequently, there was no need to clean after demolding, which greatly shortened the process flow. The demolding process was repeated five times, and the mold was still as clean as new (Fig. 5Ciii).

In order to conduct a comprehensive analysis of the process window, we chose GM30 to GM5M, with a sequential increase in mechanical properties but a decrease in biological properties, for the demolding test (Fig. 5E). The integrity of hydrogel samples is affected by the stripping process, so the same method was used to demold all the hydrogel samples, that is, stripping the hydrogel from one side, as in the simulation analysis. We found that regardless of the crosslinking method or pulling method, we could not successfully demold 5% GM30. For TPGelMA, the lower limit of the process window was 7% GM30. In this situation, TPGelMA could be used to fabricate simple structures with a depth-to-width ratio (DWR) of less than 1.5. Because only the FP method could be used, only unidirectional parallel structures such as grooves could be demolded. But when the DWR was lower than 0.5, complex microstructures such as curves and circles also could be manufactured. In contrast, the lower limit of the process window for PGelMA was 10% GM1M, and in this situation, only simple structures with a DWR of less than 1 could be manufactured. Even for the highest strength of 10% GM5M, we could only realize the manufacturing of complex structures with a DWR less than 0.5. The highest DWR was directly related to the strength of the material. In general, the DWR of low-concentration and low-substitution hydrogels (such as 7% GM30) is about 1.5:1 and that of high-concentration and high-substitution hydrogels (10% GM1M–GM5M) can reach 4:1. Obviously, the thermal–photo-crosslinking method greatly improved the process window of GelMA demolding manufacturing. Importantly, GelMA with a low substitution rate had better biological properties, indicating a higher application value for biomedicine.

In order to verify the ability to fabricate complex structures, we constructed ladder-like structures ranging from a macroscale of 5 mm to a microscale of 10 μm (Fig. 5F). This cross-scale structure has good application value in photoelectric sensing and bionics. The traditional lithography technology usually requires multiple exposures, and this scheme reduces process complexity while ensuring high resolution. Figures 5G and 5H shows the ring array and curve array structures, respectively. A multistage bifurcation vascular structure has often been used to build tumor migration models and simulate the microenvironment in vivo [65]. Figure 5I shows the three-level bifurcation vascular structure from 80 to 10 μm, and Fig. S1 (Supplementary Information) shows the microneedle structure.

The contact-guidance effect based on micropatterned hydrogels

Thermal–photo-crosslinking maintains the biocompatibility of gelatin-based hydrogels to the greatest extent while improving mechanical strength. This is because the cell adhesion sites on the collagen molecular chain are not destroyed. To verify this, we inoculated cardiomyocytes, tendon stem cells, and fibroblasts on PGelMA (Figs. 6Ai, 6Aii and 6Aiii) and TPGelMA (Figs. 6Bi, 6Bii and 6Biii), and performed LIVE/DEAD analysis on the third day. The results showed that different cells had good bioactivity on two kinds of hydrogels. To verify the contact-guidance effect of micropatterned hydrogel on cells, we constructed parallel stripe patterns (Fig. 6C) using tendon stem cells and constructed ring patterns (Figs. 6Di and 6Dii) using cardiomyocytes. It was evident that the nuclei were arranged according to the designed pattern, and the cytoskeleton also grew along the direction of the microstructures. In contrast, the hydrogels with demolding failure had hardly any influence in patterning the cells (Fig. S2 in Supplementary Information).

Microstructures of different scales and hardness have different effects on cell behavior. Generally speaking, structures close to the cell size have an obvious contact-guidance effect [3, 9, 10]. We used hydrogels with parallel microgrooves of different size and hardness to conduct "contact guidance" experiments on fibroblasts (Figs. 6Ei, 6Eii and 6Eiii, Fig. S3 in Supplementary Information). The results showed that the groove structure with a width of 10 μm, which was equivalent to the size of fibroblasts, had the best orientation effect on fibroblasts. At the same time, higher hardness was conducive to the orientational growth of fibroblasts. It may be that softer materials are more prone to deformation and degraded faster during cell culture (Fig. S4 in Supplementary Information).

Construction of micropatterned cardiomyocytes

Because hydrogels have excellent biological properties and are very soft, they are conducive to cell growth. On patterned hydrogels, cells can grow rapidly and interconnect into a network. These cell patterns on hydrogels can form a microenvironment more consistent with the actual situation in vivo (Fig. 7A).

To further verify the biological function of micropatterned cells, we analyzed the beating and functional protein expression of cardiomyocytes. Fluorescence microscopy (Fig. 7Bi), light microscopy (Fig. 7Bii), and electron microscopy (Fig. 7Biii) of cardiomyocytes in the control group showed that the cells grew in a disorderly fashion and were distributed randomly. The connections between cells were also very messy. In contrast, the cardiomyocytes in the experimental group were arranged more regularly (Fig. 7Fi). Light microscopy (Fig. 7Fii) and electron microscopy (Fig. 7Fiii)

also clearly showed that cells connected to form a more orderly network.

The video analysis software ImageJ was used to assess the beating of cardiomyocytes and showed that the beating speed was 24 BPM in the control group (Fig. 7C, Video S1 in Supplementary Information), which was an order of magnitude slower than the beating speed in the organism. The beating speed of cardiomyocytes in the experimental group was 216 BPM (Fig. 7G, Video S2 in Supplementary Information). In the experimental group, not only was the beating speed of cells increased 10 times, but beating consistency was greatly improved. Cell contraction time, peak-to-peak time, peak time, and relaxation time in the control group were longer (Fig. 7E). Moreover, the data tolerance was almost the same as the average value, which showed that the regularity of cell beating was very poor. In the experimental group, the tolerance of cell-beating data was only about one-tenth of the mean value (Fig. 7I). This showed that cells not only beat faster but also beat more regularly. A staining analysis with sarcomeric alpha actinin showed that the micropatterned cardiomyocytes had the sarcomere structure, which was distributed longitudinally along with the cells (Figs. 7Hi, 7Hii and 7Hiii). This is more in line with the actual situation in the organism. In contrast, actin in the control group was disorganized (Figs. 7Di, 7Dii and 7Diii). This showed that the patterned cardiomyocytes were closer to the real state of the organism in structure and function, which is very significant for understanding cell behavior and constructing artificial biological tissue.

Discussion

Based on the thermal response properties of gelatin-based hydrogels, we attempted a microstructural fabrication method of ultra-soft hydrogels for cell patterning. This method extended the process window, enabling the fabrication of a range of microstructures from high-concentration, high-substitution hydrogels to low-concentration, low-substitution hydrogels. However, it should be noted that this method still posed difficulties for fabrication of hydrogels with a concentration of 5%. Perhaps surface modification of the mold could solve this problem. In fact, the two major factors that affect the demolding process are the strength of the material itself and the properties of the interface. Surface modification is also an effective way to improve the release process of ultra-soft hydrogels. Mold surface modification can effectively reduce bond strength and thus material damage. We measured the tensile/shear strength (collectively referred to as mechanical strength) and adhesive strength of hydrogels fabricated by traditional and novel methods; see Figs. 3Aii–3Dii, respectively. The results showed that the mechanical strength and adhesive strength of the hydrogels prepared by the new method were improved, but the improvement in mechanical strength was greater, which made the demolding process easier. Conceivably, the use of surface modifications (such as plasma treatment) to reduce adhesive strength would have the same effect. However, it should be noted that the surface treatment method is usually not durable enough, and the effect is reduced after several repeated demolding processes. Therefore, research is still needed on how to realize fabrication of ultra-low concentration hydrogels.

In addition, we tried some other commonly used hydrogels for demolding manufacturing, such as F127DA, HAMA, and PEGDA. The results showed that 10% concentrations of F127DA and HAMA can be successfully demolded without additional treatment due to their own sufficient strength (Figs. S6A and S6B in Supplementary Information). However, when the concentration is further reduced, some problems may arise. The very soft and brittle nature of PEGDA makes it difficult to fabricate high-precision microstructures at high concentrations (Fig. S6C in Supplementary Information). Therefore, a persistent challenge is finding a way to achieve high-precision fabrication of some soft and brittle hydrogels without thermal response.

Conclusions

In summary, we propose a thermal–photo-crosslinking method to realize hydrogel surface microstructure demolding manufacturing with high precision. First, the male mold is fabricated by high-precision DLP printing. Then, the flexible female mold is cast by PDMS. Finally, thermal–photo-crosslinked gelatin-based hydrogels can be stripped from the mold without damage. Mechanical tests showed that Young's modulus and tensile strength of TPGelMA were significantly improved with this approach. In addition, LIVE/DEAD experiments on a variety of cells verified high cell livability (>80%) on TPGelMA hydrogels. The simulation and experimental results showed that structural damage in the demolding process is significantly reduced by using the thermal–photo-crosslinking method. Various patterned, bionic, and cross-scale microstructures with feature sizes of 6–80 μm were fabricated by this method. Finally, different cell patterns were achieved by adjusting microstructure size. The cardiomyocyte patterns produced a large area of fast and regular beating. Moreover, the protein expression and cell morphology were closer to the real situation in vivo. We believe that the soft-hydrogel microstructure-fabrication method described here has important potential for tissue engineering and regenerative medicine, because it could provide a universal platform for biomimetic tissue, organs-on-a-chip, cell ethology, and microfluidics.

Table 1 Abbreviations of different types of GelMA

Abbreviation	GM30	GM60	GM90	GM1M	GM3M	GM5M
Model	EFL-GM-30	EFL-GM-60	EFL-GM-90	EFL-GM100-M1	EFL-GM100-M3	EFL-GM100-M5
Degree of substitution	30% ($-NH_2$) 0% (−OH)	60% ($-NH_2$) 0% (−OH)	90% ($-NH_2$) 0% (−OH)	100% ($-NH_2$) 10% (−OH)	100% ($-NH_2$) 30% (−OH)	100% ($-NH_2$) 50% (−OH)

Experimental section

Material preparation

The following abbreviations (Table 1) were used to refer to different types of GelMA (Suzhou Intelligent Manufacturing Research Institute, Suzhou, China). From GM30 to GM5M, the substitution rate of the MA group on the gelatin molecular chain increased gradually (Fig. S5 in Supplementary Information).

GelMA solutions of different concentrations were dissolved in PBS (Qizhenhu Biological Technology Co., Ltd., Hangzhou, China) according to mass volume ratio, and 0.5% (w/v) lithium phenyl-2, 4, 6-trimethylbenzoylphosphinate (LAP) was added. Then, the solution was placed in a water bath at 50 °C for 1 h to fully dissolve the solute.

High-resolution DLP printing device and parameters

We used an ultra-high-precision DLP printer (S130, BMF Nano Material Technology Co., Ltd., Chongqing, China) to print the resin male mold with precision microstructures (HTL, BMF Nano Material Technology Co., Ltd., Chongqing, China). For the base part of the mold, the exposure intensity, exposure time, and slice layer height were set to 40, 4 s, and 40 μm, respectively. For parts with microstructure, the exposure intensity, exposure time, and slice layer height were set to 50, 0.3–0.5 s, and 5 μm, respectively.

Casting of PDMS mold

95% ethanol solution was used for ultrasonic cleaning of resin molds for 5 s, and then, fluorinated liquid (MX056, Suzhou Pengrui Nano Technology Co., Ltd., Suzhou, China) was used to ultrasonic clean molds for 5 s a second time. The cleaned resin mold was placed in an oven at 80 °C for 1 h. Subsequently, the resin mold was irradiated with a high-power 405-nm UV lamp (353,536, Jingshang Lighting Technology Co., Ltd., Ningbo, China) for 3 min as a post-curing treatment. Finally, the above steps were repeated two more times.

The PDMS (Sylgard 184, DOW Chemical Company, Midland, USA) main agent and catalyst were mixed at a mass ratio of 10:1 and poured into the resin mold, which was then placed in an 80 °C oven to cure for 30 min.

Mechanical and swelling tests, FTIR, and CD analysis

Unless otherwise specified, for the preparation of PGelMA specimens, GelMA solution was fully cured by irradiation with a high-power UV lamp for 40 s at 37 °C. To prepare TPGelMA specimens, GelMA solution was placed in a 4 °C refrigerator for pre-cooling for 5 min and then cured under the same light conditions.

In the tensile test, PGelMA specimens were printed by a biological DLP printer (EFL-BP8600, Suzhou Intelligent Manufacturing Research Institute, Suzhou, China). TPGelMA specimens were fabricated by casting GelMA solution in the PDMS mold. Both kinds of specimens had the same size and structure. The thickness, width, and length of the tensile part were 1, 2, and 12 mm, respectively. The specimens were tested with a 20-N force sensor on a universal testing machine (UTM2102, Shenzhen Suns Technology Stock Co., Ltd., Shenzhen, China) at a constant tensile rate of 10 mm/min, and the data were drawn as a tensile stress–strain curve. The slope of the linear region of the stress–strain curve corresponding to 0%–20% strain was taken as the Young's modulus.

In the shear test, the resin sheets were first printed as auxiliary fixtures. For PGelMA specimens, a small amount of solution was dropped onto the resin fixture with a rubber-head dropper. Then, another resin clamp was placed alternately, making the length and width of the overlapping area 5 and 10 mm, respectively. Finally, the PGelMA was cured with UV light. TPGelMA was pre-cooled and cured in the same way. The specimens were tested with a 20-N force sensor on a universal testing machine at a constant tensile rate of 2 mm/min, and the data were drawn as a stress–strain curve.

In the normal and tangential adhesion test, a DLP printer was first used to print the resin fixtures. Then, the PDMS base plate was fixed. A small amount of GelMA solution was dropped onto the PDMS base plate and then the resin fixture was covered, making the length and width of the contact area 5 and 10 mm, respectively. Finally, TPGelMA and PGelMA specimens were prepared in the way described. The specimens were tested with a 20-N force sensor on a universal testing machine at a constant tensile rate of 2 mm/min. The resin clamp was pulled away from the substrate in normal and tangential directions, and the data were drawn as stress-displacement curves.

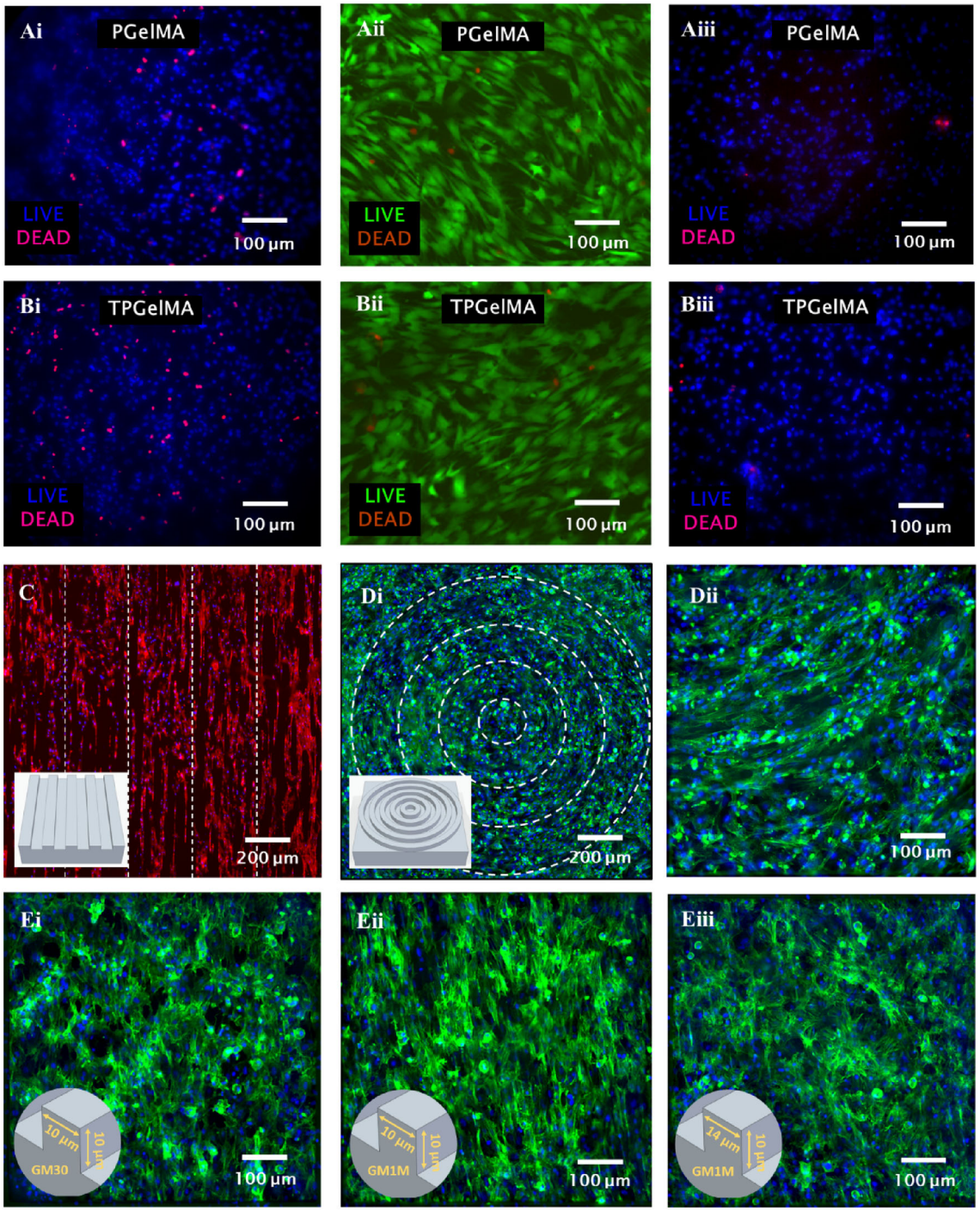

Fig. 6 Contact-guidance effect of different cells on micropatterned hydrogels. LIVE/DEAD analysis of cardiomyocytes **Ai**, tendon stem cells **Aii**, and fibroblasts **Aiii** seeded on PGelMA on the third day. LIVE/DEAD analysis of cardiomyocytes **Bi**, tendon stem cells **Bii**, and fibroblasts **Biii** seeded on TPGelMA on the third day. **C** Parallel stripe pattern constructed by tendon stem cells. **D** Ring pattern constructed by cardiomyocytes. **E** Effects of micropatterns of different sizes and materials on fibroblast orientation

Ten percent (w/v) of GM30 solution was used for swelling tests. Cylindrical specimens with a diameter of 7 mm and thickness of 5 mm were prepared by two curing methods. Then, they were placed in 75% ethanol solution, PBS, and deionized water for 2 h. Finally, the diameter of the specimens was measured under the optical microscope. Because the hydrogel material is isotropic, its volume change is proportional to the third power of the diameter change.

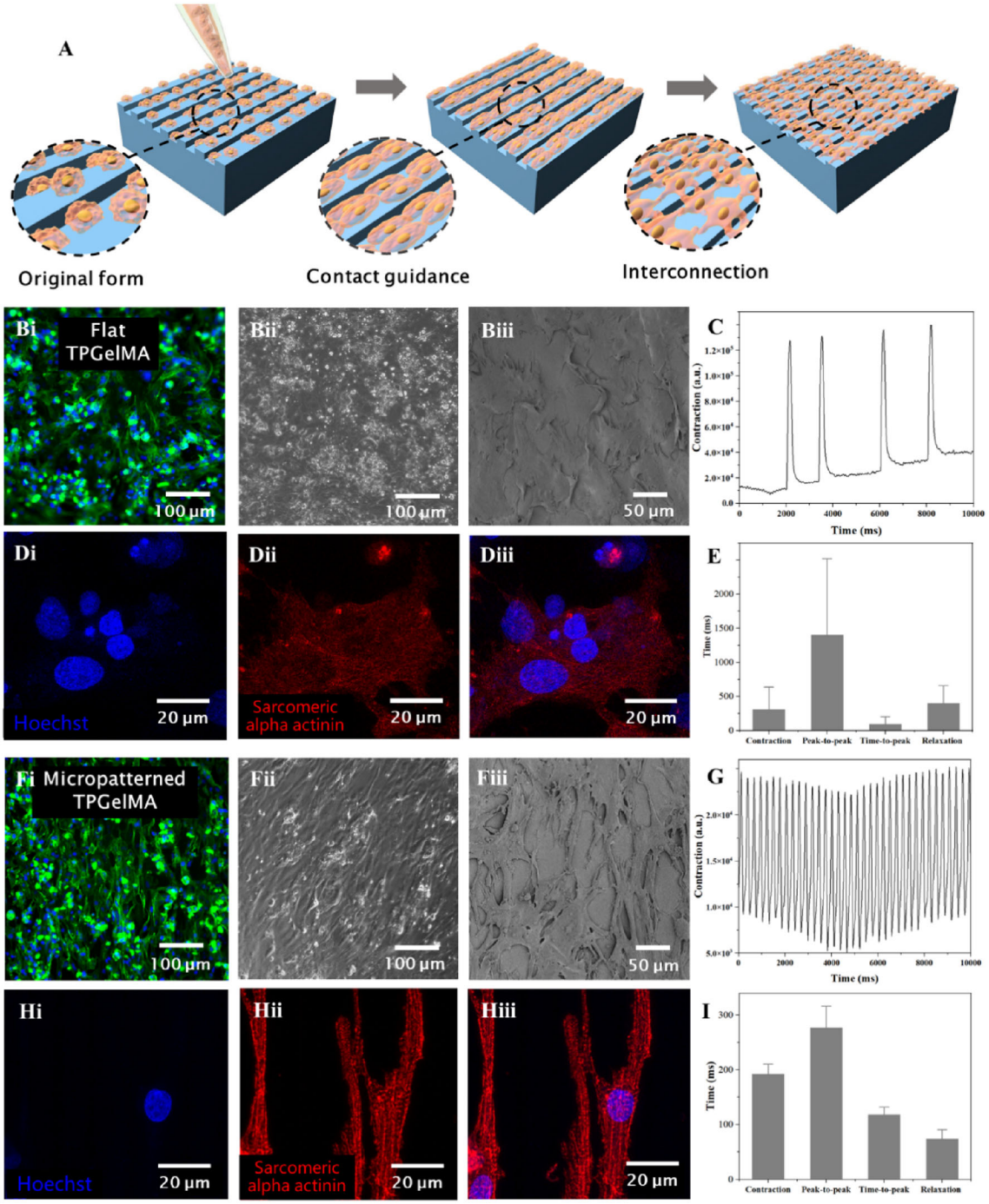

Fig. 7 Beating and protein expression of cardiomyocytes on micropatterned and flat hydrogels. **A** Cells were seeded on micropatterned hydrogels to simulate their real situation in vivo. Fluorescence microscopy **Bi**, light microscopy **Bii**, electron microscopy **Biii**, sarcomeric alpha actin staining analysis **D**, and cell-beating analysis **C** and **E** of cardiomyocytes on flat hydrogels. Fluorescence microscopy **Fi**, light microscopy **Fii**, electron microscopy **Fiii**, sarcomeric alpha actin staining analysis **H**, and cell-beating analysis **G** and **I** of cardiomyocytes on micropatterned hydrogels

GM1M was dissolved in pure water at a mass/volume ratio of 15%, and then, TPGelMA and PGelMA samples were prepared for FTIR analysis. First, the FTIR spectrum of pure water was used as the benchmark; then, the colloidal GelMA sample was placed on the FTIR spectrometer (Vertex 70, Bruker Scientific Instruments Co., Ltd., Germany) to scan the spectrum. The spectral data interval was 0.5 cm^{-1}.

0.02% (w/v) GM30, GM60, and GM90 were dissolved in pure water. The CD spectra from 230 to 190 nm were recorded at 20 °C using a spectropolarimeter (J-1500-150ST, JASCO Corporation, Japan) with a 1-cm-path-length cuvette. Then the GM30 solution was heated to 37 °C in a water bath and the CD spectrum was measured again.

Simulation analysis

ABAQUS software (Dassault Systemes, France) was employed to simulate the demolding process with different crosslinking methods and pulling directions. The model with parallel groove structures was established, and the mechanical data for TPGelMA and PGelMA were input. We used explicit dynamic analysis. The interfacial viscous behavior was defined by the contact plane interaction, and the harmonic mean stress limit was used as the damage criterion. Four-core parallel operation was used to improve the operation speed.

Cell culture and seeding on micropatterned hydrogel

Micropatterned GelMA tablets were placed in high-glucose Dulbecco's modified Eagle medium (HG DMEM) (10–013-CV, Corning, USA) and soaked at 4 °C overnight. Then, the cells were dissociated from the culture dish with 0.25% trypsin (25–051-C1, Corning, USA) for 10 min. The 10-μL cell suspension and 10-μL Trypan blue solution (T10282, Invitrogen, USA) were mixed and injected into the cell-counting plate and counted with a cell counter. The cell suspension was prepared in different concentrations. The GelMA tablets were washed with HG DMEM three times and transferred to a 48-well plate with the striped side up. Then, 450 μL of HG DMEM and 50 μL of cell suspension were added to each well successively. Tendon stem cells (CP-M176, Procell Life Science Technology Co., Ltd., Wuhan, China) were subjected to the same procedure.

Cell viability analysis

Calcein AM/PI reagent (Beyotime Biotechnology Co., Ltd., Shanghai, China) was used for the cell LIVE/DEAD assay. First, the cell-laden hydrogel chips were washed with PBS for three times. Then, Calcein AM and PI were diluted with PBS at a ratio of 500:1 and mixed evenly in the dark. Each hydrogel chip was fully soaked in 1 mL staining solution and incubated at 4 °C in the dark for 30 min. Finally, after washing with PBS, hydrogel chips were detected by fluorescence microscopy (OLYMPUS FV3000). The excitation wavelengths of living and dead cells were 488 and 545 nm, respectively.

Cell morphology analysis

F-actin and nucleus were stained to analyze cell morphology. First, the cell-laden hydrogel chips were washed with PBS for three times and fixed with 4% paraformaldehyde solution for 30 min. After that, samples were washed with PBS again. Then, rhodamine staining solution (Beyotime Biotechnology Co., Ltd., Shanghai, China) and DAPI staining solution (Beyotime Biotechnology Co., Ltd., Shanghai, China) were diluted with PBS at a ratio of 500:1. Each hydrogel chip was fully infiltrated with 0.3 mL Rhodamine staining solution and incubated at 4 °C in the dark for 8 h. Then, hydrogel chips were cleaned with PBS and stained with DAPI for 8 h in the dark. Finally, the chips were washed with PBS and imaged using a fluorescence microscope (OLYMPUS FV3000).

Cardiomyocyte beating analysis

We used an automated open-source software tool (MUSCLEMOTION) [66] to analyze the beating of cardiomyocytes. First, the recorded video of cardiomyocytes beating was divided into TIFF format image sequence at a frame rate of 30. Then, MUSCLEMOTION software was used to analyze the image sequence. The frame rate option was set to 30, and the other options were set to the default.

Scanning electron microscope (SEM) analysis

For micropatterned hydrogel with cells, first, the samples were fixed with 4% paraformaldehyde (Solarbio Co., Ltd., Shanghai, China) for 8 h at room temperature. Then, they were rinsed three times with PBS and soaked for 15 min each time. Subsequently, 1% osmic acid solution (Structure Probe, Inc, USA) was used for secondary fixation for 1 h. Finally, for dehydration, the samples were soaked in a series of ethanol solutions (30%, 50%, 70%, 80%, 90%, 95%, and 100%) for 15 min each time. After that, the samples were critical-point dried. Finally, they were coated with platinum and imaged in the SEM system (SU-8010, Hitachi Co., Ltd., Japan).

Supplementary Information The online version contains supplementary material available at https://doi.org/10.1007/s42242-022-00207-1.

Acknowledgements The authors acknowledge the Bio-Ultrastructure Analysis Laboratory of Analysis Center of Agrobiology and Environmental Sciences with scanning electron microscopy and confocal microscopy. This study was sponsored by the National Key Research and Development Program of China (No. 2018YFA0703000) and the National Natural Science Foundation of China (Nos. T2121004 and U1909218). YW was supported by the Innovation Team and Talents Cultivation Program of National Administration of Traditional Chinese Medicine (No. ZYYCXTD-D-202002).

Author contributions CFH provided conceptualization, data curation, methodology, formal analysis, investigation, writing—original draft. XCC did data curation, investigation, resources, software, methodology, formal analysis. YS contributed to methodology, formal analysis, software. MJX was involved in investigation and visualization. KY contributed to visualization and data curing. JH did resources and data curing. JWL investigated the study. QG did resources. JN contributed to visualization. YW and YH were involved in supervision, resources, project administration, writing—review and editing.

Declarations

Conflict of interest The authors declare that they have no conflict of interest.

Ethical approval This study does not contain any work related to human subjects performed by any of the authors. All experiments were executed following the guild for the Care and Use of Laboratory Animals published by the US National Institutes of Health (NIH Publication No.85–23, revised 1996) and the protocols were approved by the Institutional Animal Care and Use Committee of Zhejiang University.

References

1. Chen S, Shi X, Chinnathambi S et al (2013) Generation of microgrooved silica nanotube membranes with sustained drug delivery and cell contact guidance ability by using a Teflon microfluidic chip. Sci Technol Adv Mater 14(1):015005. https://doi.org/10.1088/1468-6996/14/1/015005
2. Leclech C, Villard C (2020) Cellular and subcellular contact guidance on microfabricated substrates. Front Bioeng Biotechnol 8:551505. https://doi.org/10.3389/fbioe.2020.551505
3. Nguyen AT, Sathe SR, Yim EK (2016) From nano to micro: topographical scale and its impact on cell adhesion, morphology and contact guidance. J Phys Condens Matter 28(18):183001. https://doi.org/10.1088/0953-8984/28/18/183001
4. Ferraris S, Spriano S, Scalia AC et al (2020) Topographical and biomechanical guidance of electrospun fibers for biomedical applications. Polymers 12(12):2896. https://doi.org/10.3390/polym12122896
5. Charest JL, García AJ, King WP (2007) Myoblast alignment and differentiation on cell culture substrates with microscale topography and model chemistries. Biomaterials 28(13):2202–2210. https://doi.org/10.1016/j.biomaterials.2007.01.020
6. Loesberg WA, te Riet J, van Delft FC et al (2007) The threshold at which substrate nanogroove dimensions may influence fibroblast alignment and adhesion. Biomaterials 28(27):3944–3951. https://doi.org/10.1016/j.biomaterials.2007.05.030
7. Biggs MJ, Richards RG, McFarlane S et al (2008) Adhesion formation of primary human osteoblasts and the functional response of mesenchymal stem cells to 330 nm deep microgrooves. J R Soc Interf 5(27):1231–1242. https://doi.org/10.1098/rsif.2008.0035
8. Teixeira AI, Abrams GA, Bertics PJ et al (2003) Epithelial contact guidance on well-defined micro- and nanostructured substrates. J Cell Sci 116(Pt 10):1881–1892. https://doi.org/10.1242/jcs.00383
9. Ermis M, Antmen E, Hasirci V (2018) Micro and nanofabrication methods to control cell-substrate interactions and cell behavior: a review from the tissue engineering perspective. Bioact Mater 3(3):355–369. https://doi.org/10.1016/j.bioactmat.2018.05.005
10. Simitzi C, Karali K, Ranella A et al (2018) Controlling the outgrowth and functions of neural stem cells: the effect of surface topography. ChemPhysChem 19(10):1143–1163. https://doi.org/10.1002/cphc.201701175
11. Xie C, Gao Q, Wang P et al (2019) Structure-induced cell growth by 3D printing of heterogeneous scaffolds with ultrafine fibers. Mater Des 181:108092. https://doi.org/10.1016/j.matdes.2019.108092
12. Rezaei Nejad H, Goli Malekabadi Z, Kazemzadeh Narbat M et al (2016) Laterally confined microfluidic patterning of cells for engineering spatially defined vascularization. Small 12(37):5132–5139. https://doi.org/10.1002/smll.201601391
13. Sun Y, Yu K, Nie J et al (2020) Modeling the printability of photocuring and strength adjustable hydrogel bioink during projection based 3D bioprinting. Biofabrication 13(3):035032. https://doi.org/10.1088/1758-5090/aba413
14. Henning AK, Fitch JS, Harris JM et al (1998) Microfluidic MEMS for semiconductor processing. IEEE Trans Components Packag Manuf Technol Part B 21(4):329–337. https://doi.org/10.1109/96.730416
15. Rodriguez I, Spicar-Mihalic P, Kuyper CL et al (2003) Rapid prototyping of glass microchannels. Anal Chim Acta 496(1–2):205–215. https://doi.org/10.1016/S0003-2670(03)01000-6
16. Vasiev I, Greer AIM, Khokhar AZ et al (2013) Self-folding nano- and micropatterned hydrogel tissue engineering scaffolds by single step photolithographic process. Microelectron Eng 108:76–81. https://doi.org/10.1016/j.mee.2013.04.003
17. Jeong HE, Kwak R, Kim JK et al (2008) Generation and self-replication of monolithic, dual-scale polymer structures by two-step capillary-force lithography. Small 4(11):1913–1918. https://doi.org/10.1002/smll.200800151
18. Cutiongco MFA, Goh SH, Aid-Launais R et al (2016) Planar and tubular patterning of micro and nano-topographies on poly(vinyl alcohol) hydrogel for improved endothelial cell responses. Biomaterials 84:184–195. https://doi.org/10.1016/j.biomaterials.2016.01.036
19. Kane RS, Takayama S, Ostuni E et al (1999) Patterning proteins and cells using soft lithography. Biomaterials 20(23–24):2363–2376. https://doi.org/10.1016/s0142-9612(99)00165-9
20. Xia Y, Whitesides GM (1998) Soft lithography. Angew Chem Int Ed 37(5):550–575. https://doi.org/10.1002/(SICI)1521-3773(19980316)37:5%3c550::AID-ANIE550%3e3.0.CO;2-G
21. Agarwal A, Farouz Y, Nesmith AP et al (2013) Micropatterning alginate substrates for in vitro cardiovascular muscle on a chip. Adv Funct Mater 23(30):3738–3746. https://doi.org/10.1002/adfm.201203319
22. Lawrence BD, Marchant JK, Pindrus MA et al (2009) Silk film biomaterials for cornea tissue engineering. Biomaterials 30(7):1299–1308. https://doi.org/10.1016/j.biomaterials.2008.11.018
23. Nikkhah M, Eshak N, Zorlutuna P et al (2012) Directed endothelial cell morphogenesis in micropatterned gelatin methacrylate hydrogels. Biomaterials 33(35):9009–9018. https://doi.org/10.1016/j.biomaterials.2012.08.068
24. Annabi N, Tsang K, Mithieux SM et al (2013) Highly elastic micropatterned hydrogel for engineering functional cardiac tissue. Adv Funct Mater 23(39):4950–4959. https://doi.org/10.1002/adfm.201300570
25. Golden AP, Tien J (2007) Fabrication of microfluidic hydrogels using molded gelatin as a sacrificial element. Lab Chip 7(6):720–725. https://doi.org/10.1039/b618409j
26. Müller E, Pompe T, Freudenberg U et al (2017) Solvent-assisted micromolding of biohybrid hydrogels to maintain human hematopoietic stem and progenitor cells ex vivo. Adv Mater 29(42):1703489. https://doi.org/10.1002/adma.201703489
27. Lv S, Nie J, Gao Q et al (2020) Micro/nanofabrication of brittle hydrogels using 3D printed soft ultrafine fiber molds for damage-free demolding. Biofabrication 12(2):025015. https://doi.org/10.1088/1758-5090/ab57d8

28. Pepelanova I, Kruppa K, Scheper T et al (2018) Gelatin-methacryloyl (GelMA) hydrogels with defined degree of functionalization as a versatile toolkit for 3D cell culture and extrusion bioprinting. Bioengineering 5(3):55. https://doi.org/10.3390/bioengineering5030055
29. Schuurman W, Levett PA, Pot MW et al (2013) Gelatin-methacrylamide hydrogels as potential biomaterials for fabrication of tissue-engineered cartilage constructs. Macromol Biosci 13(5):551–561. https://doi.org/10.1002/mabi.201200471
30. Schipani R, Scheurer S, Florentin R et al (2020) Reinforcing interpenetrating network hydrogels with 3D printed polymer networks to engineer cartilage mimetic composites. Biofabrication 12(3):035011. https://doi.org/10.1088/1758-5090/ab8708
31. Vila A, Torras N, Castaño AG et al (2020) Hydrogel co-networks of gelatine methacrylate and poly(ethylene glycol) diacrylate sustain 3D functional in vitro models of intestinal mucosa. Biofabrication 12(2):025008. https://doi.org/10.1088/1758-5090/ab5f50
32. Zhang Y, Chen M, Tian J et al (2019) In situ bone regeneration enabled by a biodegradable hybrid double-network hydrogel. Biomater Sci 7(8):3266–3276. https://doi.org/10.1039/c9bm00561g
33. Wang H, Zhou L, Liao J et al (2014) Cell-laden photocrosslinked GelMA-DexMA copolymer hydrogels with tunable mechanical properties for tissue engineering. J Mater Sci Mater Med 25(9):2173–2183. https://doi.org/10.1007/s10856-014-5261-x
34. Shoulders MD, Raines RT (2009) Collagen structure and stability. Annu Rev Biochem 78:929–958. https://doi.org/10.1146/annurev.biochem
35. Marini JC, Forlino A, Cabral WA et al (2007) Consortium for osteogenesis imperfecta mutations in the helical domain of type I collagen: regions rich in lethal mutations align with collagen binding sites for integrins and proteoglycans. Hum Mutat 28(3):209–221. https://doi.org/10.1002/humu.20429
36. Kirkness MW, Lehmann K, Forde NR (2019) Mechanics and structural stability of the collagen triple helix. Curr Opin Chem Biol 53:98–105. https://doi.org/10.1016/j.cbpa.2019.08.001
37. Rizwan M, Peh GSL, Ang HP et al (2017) Sequentially-crosslinked bioactive hydrogels as nano-patterned substrates with customizable stiffness and degradation for corneal tissue engineering applications. Biomaterials 120:139–154. https://doi.org/10.1016/j.biomaterials.2016.12.026
38. Young AT, White OC, Daniele MA (2020) Rheological properties of coordinated physical gelation and chemical crosslinking in gelatin methacryloyl (GelMA) hydrogels. Macromol Biosci 20(12):e2000183. https://doi.org/10.1002/mabi.202000183
39. Van Den Bulcke AI, Bogdanov B et al (2000) Structural and rheological properties of methacrylamide modified gelatin hydrogels. Biomacromol 1(1):31–38. https://doi.org/10.1021/bm990017d
40. Kapoor N, Liang W, Marbán E et al (2013) Direct conversion of quiescent cardiomyocytes to pacemaker cells by expression of Tbx18. Nat Biotechnol 31(1):54–62. https://doi.org/10.1038/nbt.2465
41. Wells SP, Waddell HM, Sim CB et al (2019) Cardiomyocyte functional screening: interrogating comparative electrophysiology of high-throughput model cell systems. Am J Physiol Cell Physiol 317(6):C1256–C1267. https://doi.org/10.1152/ajpcell.00306.2019
42. Sathaye A, Bursac N, Sheehy S et al (2006) Electrical pacing counteracts intrinsic shortening of action potential duration of neonatal rat ventricular cells in culture. J Mol Cell Cardiol 41(4):633–641. https://doi.org/10.1016/j.yjmcc.2006.06.076
43. Quan D, Huang H (2018) In vitro study of the effects of reprogramming neonatal rat fibroblasts transfected with TBX18 on spontaneous beating in neonatal rat cardiomyocytes. Mol Med Rep 18(6):5520–5526. https://doi.org/10.3892/mmr.2018.9566
44. Yue K, Li X, Schrobback K et al (2017) Structural analysis of photocrosslinkable methacryloyl-modified protein derivatives. Biomaterials 139:163–171. https://doi.org/10.1016/j.biomaterials.2017.04.050
45. Sigen A, Zeng M, Johnson M et al (2020) Green synthetic approach for photo-cross-linkable methacryloyl hyaluronic acid with a tailored substitution degree. Biomacromol 21(6):2229–2235. https://doi.org/10.1021/acs.biomac.0c00196
46. Farokhi M, Shariatzadeh FJ, Solouk A et al (2020) Alginate based scaffolds for cartilage tissue engineering: a review. Int J Polym Mater Polym Biomat 69(4):230–247. https://doi.org/10.1016/j.ijbiomac.2014.07.008
47. Qi Y, Li KY, Zhao CW et al (2021) Preparation of a poly (PEGDA-*co*-GMA) thin hydrogel matrix for oligonucleotide microarray applications. J Chem Technol Biotechnol 96(7):1902–1908. https://doi.org/10.1002/jctb.6709
48. Liu X, Sun Y, Chen B et al (2022) Novel magnetic silk fibroin scaffolds with delayed degradation for potential long-distance vascular repair. Bioact Mater 7:126–143. https://doi.org/10.1016/j.bioactmat.2021.04.036
49. Liu Y, Chan-Park MB (2010) A biomimetic hydrogel based on methacrylated dextran-graft-lysine and gelatin for 3D smooth muscle cell culture. Biomaterials 31(6):1158–1170. https://doi.org/10.1016/j.biomaterials.2009.10.040
50. Van den Steen PE, Dubois B, Nelissen I et al (2002) Biochemistry and molecular biology of gelatinase B or matrix metalloproteinase-9 (MMP-9). Crit Rev Biochem Mol Biol 37(6):375–536. https://doi.org/10.1080/10409230290771546
51. Yue K, Trujillo-de Santiago G, Alvarez MM et al (2015) Synthesis, properties, and biomedical applications of gelatin methacryloyl (GelMA) hydrogels. Biomaterials 73:254–271. https://doi.org/10.1016/j.biomaterials.2015.08.045
52. Nichol JW, Koshy ST, Bae H et al (2010) Cell-laden microengineered gelatin methacrylate hydrogels. Biomaterials 31(21):5536–5544. https://doi.org/10.1016/j.biomaterials.2010.03.064
53. Li M, Song X, Jin S et al (2020) 3D tumor model biofabrication. Bio-Des Manuf 4(3):526–540. https://doi.org/10.1007/s42242-021-00134-7
54. Ma L, Li Y, Wu Y et al (2020) The construction of in vitro tumor models based on 3D bioprinting. Bio-Des Manuf 3(3):227–236. https://doi.org/10.1007/s42242-020-00068-6
55. Ha M, Athirasala A, Tahayeri A et al (2020) Micropatterned hydrogels and cell alignment enhance the odontogenic potential of stem cells from apical papilla in-vitro. Dental Mater 36(1):88–96. https://doi.org/10.1016/j.dental.2019.10.013
56. Lu K, Qian Y, Gong J et al (2020) Biofabrication of aligned structures that guide cell orientation and applications in tissue engineering. Bio-Des Manuf 4(2):258–277. https://doi.org/10.1007/s42242-020-00104-5
57. Ying GL, Jiang N, Maharjan S et al (2018) Aqueous two-phase emulsion bioink-enabled 3D bioprinting of porous hydrogels. Adv Mater 30(50):e1805460. https://doi.org/10.1002/adma.201805460
58. Nie J, Gao Q, Xie C et al (2020) Construction of multi-scale vascular chips and modelling of the interaction between tumours and blood vessels. Mater Horiz 7(1):82–92. https://doi.org/10.1039/C9MH01283D
59. Peng LH, Xu XH, Huang YF et al (2020) Self-adaptive all-in-one delivery chip for rapid skin nerves regeneration by endogenous mesenchymal stem cells. Adv Funct Mater 30(40):2001751. https://doi.org/10.1002/adfm.202001751
60. Mehta V, Rath SN (2021) 3D printed microfluidic devices: a review focused on four fundamental manufacturing approaches and implications on the field of healthcare. Bio-Des Manuf 4(2):311–343. https://doi.org/10.1007/s42242-020-00112-5
61. Xie M, Gao Q, Fu J et al (2020) Bioprinting of novel 3D tumor array chip for drug screening. Bio-Des Manuf 3(3):175–188. https://doi.org/10.1007/s42242-020-00078-4

62. Greenfield NJ (2006) Using circular dichroism spectra to estimate protein secondary structure. Nat Protoc 1(6):2876–2890. https://doi.org/10.1038/nprot.2006.202
63. Fornaro T, Burini D, Biczysko M et al (2015) Hydrogen-bonding effects on infrared spectra from anharmonic computations: uracil-water complexes and uracil dimers. J Phys Chem A 119(18):4224–4236. https://doi.org/10.1021/acs.jpca.5b01561
64. Yang T, Wang C, Wu Z (2021) Strain hardening in graphene foams under shear. ACS Omega 6(35):22780–22790. https://doi.org/10.1021/acsomega.1c03127
65. Wang P, Sun Y, Shi X et al (2021) 3D printing of tissue engineering scaffolds: a focus on vascular regeneration. Bio-Des Manuf 4(2):344–378. https://doi.org/10.1007/s42242-020-00109-0
66. Sala L, van Meer BJ, Tertoolen LGJ et al (2018) Musclemotion: a versatile open software tool to quantify cardiomyocyte and cardiac muscle contraction in vitro and in vivo. Circ Res 122(3):e5–e16. https://doi.org/10.1161/CIRCRESAHA.117.312067